



RESEARCH LETTER

10.1029/2018GL078487

Key Points:

- We compare tidal magnetic signals (amplitudes and phases) from observatories compared to those from physics-based numerical models
- We present the first comparison of magnetic fields induced by TIME-GCM's physics-based ionospheric M₂ tidal electric current
- We find that predicted ionospheric M₂ Z component is very small; this is encouraging for electromagnetic sensing

Supporting Information:

- Supporting Information S1

Correspondence to:

N. R. Schnepf,
neesha.schnepf@colorado.edu

Citation:

Schnepf, N. R., Nair, M. C., Maute, A., Pedatella, N. M., Kuvshinov, A., & Richmond, A. D. (2018). A comparison of model-based ionospheric and ocean tidal magnetic signals with observational data. *Geophysical Research Letters*, 45, 7257–7267. <https://doi.org/10.1029/2018GL078487>

Received 27 APR 2018

Accepted 20 JUN 2018

Accepted article online 25 JUN 2018

Published online 3 AUG 2018

A Comparison of Model-Based Ionospheric and Ocean Tidal Magnetic Signals With Observatory Data

N. R. Schnepf^{1,2} , M. Nair^{2,3}, A. Maute⁴ , N. M. Pedatella⁴ , A. Kuvshinov⁵ ,
and A. D. Richmond⁴ 

¹Department of Geological Sciences, University of Colorado Boulder, Boulder, CO, USA, ²Cooperative Institute for Research in Environmental Sciences, University of Colorado Boulder, Boulder, CO, USA, ³National Centers for Environmental Information, National Oceanic and Atmospheric Administration, Boulder, CO, USA, ⁴High Altitude Observatory, National Center for Atmospheric Research, Boulder, CO, USA, ⁵Institute of Geophysics, ETH Zurich, Zurich, Switzerland

Abstract Observed tidal geomagnetic field variations are due to a combination of electric currents in the ionosphere, ocean, and their induced counterparts. Using these variations to constrain subsurface electrical conductivity in oceanic regions is a promising frontier; however, properly separating the ionospheric and oceanic tidal contributions of the magnetic field is critical for this. We compare semidiurnal lunar tidal magnetic signals (i.e., the signals due to the M₂ tidal mode) estimated from 64 global observatories to physics-based forward models of the ionospheric M₂ magnetic field and the oceanic M₂ magnetic field. At ground level, predicted ionospheric M₂ amplitudes are strongest in the horizontal components, whereas the predicted oceanic amplitudes are strongest in the vertical direction. There is good agreement between the predicted and estimated M₂ phases for the Y component; however, the F and X components experience deviations that may be indicative of unmodeled ionospheric processes or unmodeled coastal effects. Overall, we find that the agreement between the physics-based model predictions and the observations is very encouraging for electromagnetic sensing applications, especially since the predicted ionospheric vertical component is very weak.

Plain Language Summary Both Earth's oceans and upper atmosphere produce electric current and electromagnetic (EM) fields. Tides caused by the gravitational interaction between Earth, the Sun, and Moon create reliable, easily constrained EM signals in both the ocean and upper atmosphere. Geophysicists are interested in using these ocean tidal EM signals to study the electrical conductivity of Earth's interior; however, this requires a solid understanding of the upper atmosphere's contribution to the EM signal. This study uses a physics-based model to estimate the relative EM tidal signals of the ocean versus the upper atmosphere to immediately address this concern. We also compare the model predictions with the EM tidal signals constrained from 64 global observatories. Considering the level of complexity of the upper atmosphere's EM tidal signals, we find remarkable agreement between the observed and modeled EM tidal signals. Some of the discrepancies may be of interest to those in upper atmospheric/space physics because they may be due to unmodeled physical processes. Our results are also very encouraging for geophysicists aiming to use EM tidal signals to study Earth's interior since they suggest a small upper atmosphere contribution to the EM tidal signal generally used.

1. Introduction

Gravitational forces from the Sun and the Moon, along with periodic solar heating of the atmosphere, cause periodic motions of the ocean and atmosphere that generate electric currents. Thus, observed tidal geomagnetic variations are due to a combination of tidal electric currents in the ionosphere, ocean, and their induced counterparts. Of the various tides, the semidiurnal lunar (M₂) tidal mode (period of 12.4206 hr) is the largest lunar tide.

Electric currents within the ionosphere are produced by the ionospheric wind dynamo (Kelley, 1989; Richmond, 1995). Within the ionosphere's 100- to 120-km altitude region, where daytime Pedersen and Hall conductivities are largest, upwardly propagating atmospheric tides and waves dominate the creation of electric currents. Above this altitude, variations in solar heating drive winds and currents dominated

by periodicities of 24 hr and its harmonics. These ionospheric currents cause the well-known daily variations in the geomagnetic field.

The ionospheric M_2 magnetic signal peaks during the Northern Hemisphere's winter months (Pedatella, 2014; Stening, 2011). However, it remains unclear how much of that peak is due to seasonal atmospheric variations or to sudden stratospheric warming (SSW) events. These SSW events are due to troposphere dynamics, so their occurrence is largely random; however, they occur in the northern winter and it is established that they can increase the ionospheric M_2 electric current and thus the corresponding magnetic signal. In general, ionospheric M_2 tides are not nearly so tightly coupled to the lunar gravitational forcing as are oceanic M_2 tides. Ionospheric tides depend on atmospheric propagation conditions, including not only winter SSWs but also other atmospheric and ionospheric variations (Chau et al., 2015; Pedatella et al., 2012; Zhang & Forbes, 2013). Additionally, ionospheric magnetic signals depend on magnetospheric conditions, which affect the currents at all latitudes (Kelley, 1989). Lastly, as demonstrated by Yamazaki and Kosch (2014), ionospheric lunar tidal currents are sensitive to the solar ionizing radiation, so during a solar minimum these tidal currents are expected to have a diminished signal compared to solar maximum.

Unlike the ionospheric tidal magnetic signals, oceanic tidal magnetic signals vary insignificantly with the season or climate. Oceanic magnetic signals are generated through motional induction: As electrically conducting salt water moves through Earth's ambient magnetic field, a secondary electromagnetic (EM) field is produced. While seawater's electrical conductivity depends on salinity and temperature, seasonal changes in those parameters are minute when compared to the largely unchanged tidal transport and Earth's background magnetic field (Grayver et al., 2016; Tyler et al., 2017). Oceanic tidal magnetic signals have been detected by satellites (Sabaka et al., 2015, 2016; Tyler et al., 2003), coastal observatories (Bindoff et al., 1988; Cueto et al., 2003; Hewson-Browne, 1973; Love & Rigler, 2014; Malin, 1970; Maus & Kuvshinov, 2004; McKnight, 1995; Winch, 1970), and seafloor data (Kuvshinov et al., 2006; Schnepf et al., 2014).

Oceanic tidal magnetic signals are of special interest because they are galvanically coupled with Earth's subsurface, making them ideal for probing shallow, resistive regions of the lithosphere and mantle—regions of great geodynamic interest because of their partial melts and volatiles, and role in plate tectonics. With the recent increase in high-quality magnetic data from satellite missions (Ørsted, CHAMP, SAC-C and Swarm), there has been rising interest in probing Earth from space using signals of magnetospheric origin (Civet & Tarits, 2013; Civet et al., 2015; Kuvshinov et al., 2006; Püthe & Kuvshinov, 2013, 2014; Püthe et al., 2015; Velimský, 2010, 2013), as well as signals of tidal origin for these purposes (Schnepf et al., 2015). In fact, mapping the electrical conductivity of Earth's mantle is one of the primary scientific objectives of the *Swarm* mission (Olsen et al., 2013), and recently, there were breakthroughs in using oceanic magnetic tidal signals to probe the lithosphere and upper mantle (Grayver et al., 2016, 2017). Of note, all of these studies have focused on constraining 1-D conductivity distributions either globally or regionally (i.e., beneath oceans)—They do not delve into detecting lateral variations of conductivity.

To utilize tidal magnetic signals in EM sensing, it is necessary to be able to independently describe the electric current source when inverting for the lithospheric and upper mantle electric conductivity by minimizing the misfits between numerical models and observed data. Fortunately, this is not a problem when using the magnetic signals of oceanic tides because they have been studied through a variety of physical oceanography methods, and data-assimilated models (e.g., Egbert & Erofeeva, 2002; Taguchi et al., 2014) provide a reliable source of the tidal velocities necessary to estimate the oceanic tidal EM signals. However, using oceanic tidal magnetic signals to detect lateral variations of the conductivity of the lithosphere and upper mantle depends on improving error constraints for the observed tidal magnetic signals (Sabaka et al., 2015, 2016).

The oceanic tidal magnetic signal is generally extracted by exploiting local nighttime data under the assumption that because the nighttime ionospheric E region conductivity is an order of 2 less than its daytime value, the ionospheric contribution may be ignored (Malin, 1970). The accuracy of this assumption becomes important if tidal EM sensing is to grow from providing radial conductivity profiles to 3-D conductivity distributions. It also becomes critical to refine the ionosphere and ocean field separation when using data sources that prevent the isolation of local nighttime data. For example, while tidal signals have been determined from seafloor voltage cables (e.g., Kuvshinov et al., 2006), these cables are thousands of kilometers in length, thus often traverse many local times making it tricky to use local nighttime data. Consequently, the extracted tidal signal from these cables is a combination of oceanic and ionospheric sources. Note that cables measure electric field values, and electric fields are beyond the scope of this study.

In this paper, rather than attempting to separate the ionospheric and oceanic M_2 signals from observatory data (eg., Bindoff et al., 1988; Larsen, 1968; Larsen & Cox, 1966; Winch, 1981), we compare M_2 signals estimated from global observatories to physics-based numerical models of the ionospheric M_2 magnetic field and the oceanic M_2 magnetic field. In particular, we present the first comparison of the numerical Thermosphere Ionosphere Mesosphere Electrodynamics General Circulation Model's (TIME-GCM) predicted M_2 ionospheric magnetic signal with that of observatories. This approach enables a physics-based examination of ionospheric tidal signals versus oceanic tidal signals, thus providing information about the level of contamination of oceanic tidal signals by their ionospheric counterpart.

Section 2 discusses the analysis of observatory data, section 3 details the forward model techniques used, section 4 examines the results of the forward models, and section 5 discusses their similarities and differences to the observatory data. Finally, section 6 provides a summary and outlook for future work.

2. Analysis of Observatory Signals

2.1. Data

Hourly data from 64 nonpolar (i.e., the colatitude is between 34° and 146°) geomagnetic observatories were obtained from the British Geological Survey. We used the northward (X), eastward (Y), and downward (Z) components of the magnetic field, and the total scalar field was determined as $F = \sqrt{X^2 + Y^2 + Z^2}$.

Our study focused on 90 days during the Northern Hemisphere's summer within the 2009 solar minimum (30 May 2009 through 27 August 2009). Using this time period, we avoid the ionospheric signal being contaminated by winter SSWs and are focusing on the season when the ionospheric M_2 strength is weaker (Pedatella, 2014; Stening, 2011). By employing data from the solar minima, we minimize effects from magnetospheric conditions. In fact, during this time period, geomagnetic activity was very low with the A_p index exceeding 20 ($A_p = 24$) only on 22 July 2009 (Denig, 2015). Thus, the expected ionospheric signal may serve as the lower error bound brought in by this signal for EM sensing using the signals due to oceanic tides (Yamazaki & Kosch, 2014).

2.2. Estimation of Magnetic Tidal Modes

Following Schnepf et al. (2014), we directly fit for the 10 major tidal modes that have a period within 24 hr (i.e., S_{1-6} , K_{1-2} , M_2 , N_2 , all shown in Table S1 in the supporting information; M_2 's period is 12.421 hr) using the mathematical model given by

$$y_i = \sum_n \{A(n)\cos[2\pi\nu(n)t_i] + B(n)\sin[2\pi\nu(n)t_i]\} + C, \quad (1)$$

where y_i is a magnetic measurement (i.e., X , Y , Z , or F), $i = 1, \dots, N$ is a positive integer corresponding to each data point, n is a positive integer representing each considered tidal mode, $\nu(n)$ is the frequency of the considered tidal signal (i.e., number of cycles per day), and t is time in days. The coefficients $A(n)$, $B(n)$, and C are estimated from fitting the above model to the data by using MATLAB's *robust fit* function. Along with the estimated coefficients, this provides the corresponding standard error.

While readers are encouraged to check Schnepf et al. (2014) for details of this method, it should be noted that our method differs from theirs in two critical ways: (1) we do not fit for tidal modes greater than 24 hr in length and (2) we do not separate local daytime versus nighttime data—We use all continuous 90 days of data. By excluding periods greater than 24 hr, we are neglecting any contribution from planetary waves with periods of approximately 2, 5, 10, and 16 days, which may be present (Forbes, 1996). Additionally, combining daytime and nighttime data introduces lunisolar frequencies, which consist of sums and differences of solar and lunar frequencies, owing to the solar modulation of ionospheric conductivities that affect the lunar ionospheric currents. However, lunisolar periods are not included in our analysis.

At most stations, and for all components, the M_2 amplitudes are significantly larger than the estimated standard errors (Tables S8–S11). However, we should note that the standard error calculated from MATLAB's *robust fit* function likely underestimates the true uncertainty of the amplitudes since variations with planetary wave and lunisolar periods are not included in the modeled tidal periods. Such components are treated by the fitting function as though they were random data errors, but in reality these components have temporal coherence and are not independent from one time to the next, unlike truly random data errors.

In general, the observed M_2 amplitudes across the 64 stations range from 0.02 to 3.83 nT. The X component had the smallest range (0.07 to 1.31 nT), whereas the Z component had the largest range of 0.09 to 3.83 nT.

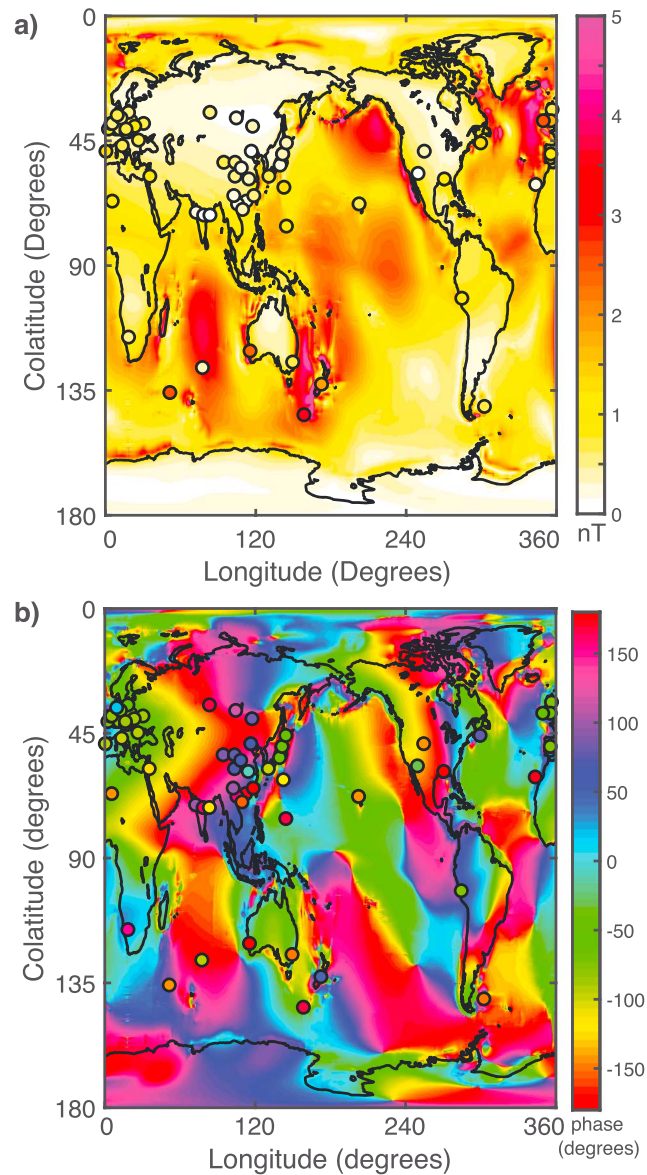


Figure 1. The background map illustrates the total scalar M_2 magnetic field (a) amplitude and (b) phase predicted from the sum of the ionosphere and ocean sources. Each colored dot represents the total M_2 scalar field amplitude and phase at a geomagnetic observatory.

The Y component's range was 0.17 to 2.41 nT, and the scalar anomaly ranged from 0.02 to 3.54 nT. All the observed M_2 amplitudes (i.e., $\sqrt{A^2 + B^2}$) are shown tabulated in the supporting information, along with their standard error.

Figure 1 shows the observed scalar anomaly's amplitude and phase at the considered stations (the colored dots), and Figure 2 shows the amplitude and phase of each component estimated at the considered stations (the colored dots). Phase was determined as $\tan^{-1}(B/A)$. The background in these figures is produced from the forward models discussed in the following section. It is worth noting that for weak amplitudes, the corresponding phase is meaningless.

3. Forward Modeling the M_2 Magnetic Signal

We simulate the EM signals due to both the M_2 oceanic tidal flow and ionospheric tidal flow utilizing the frequency domain numerical solution described in Kuvshinov (2008). This solution computes the electric (\mathbf{E})

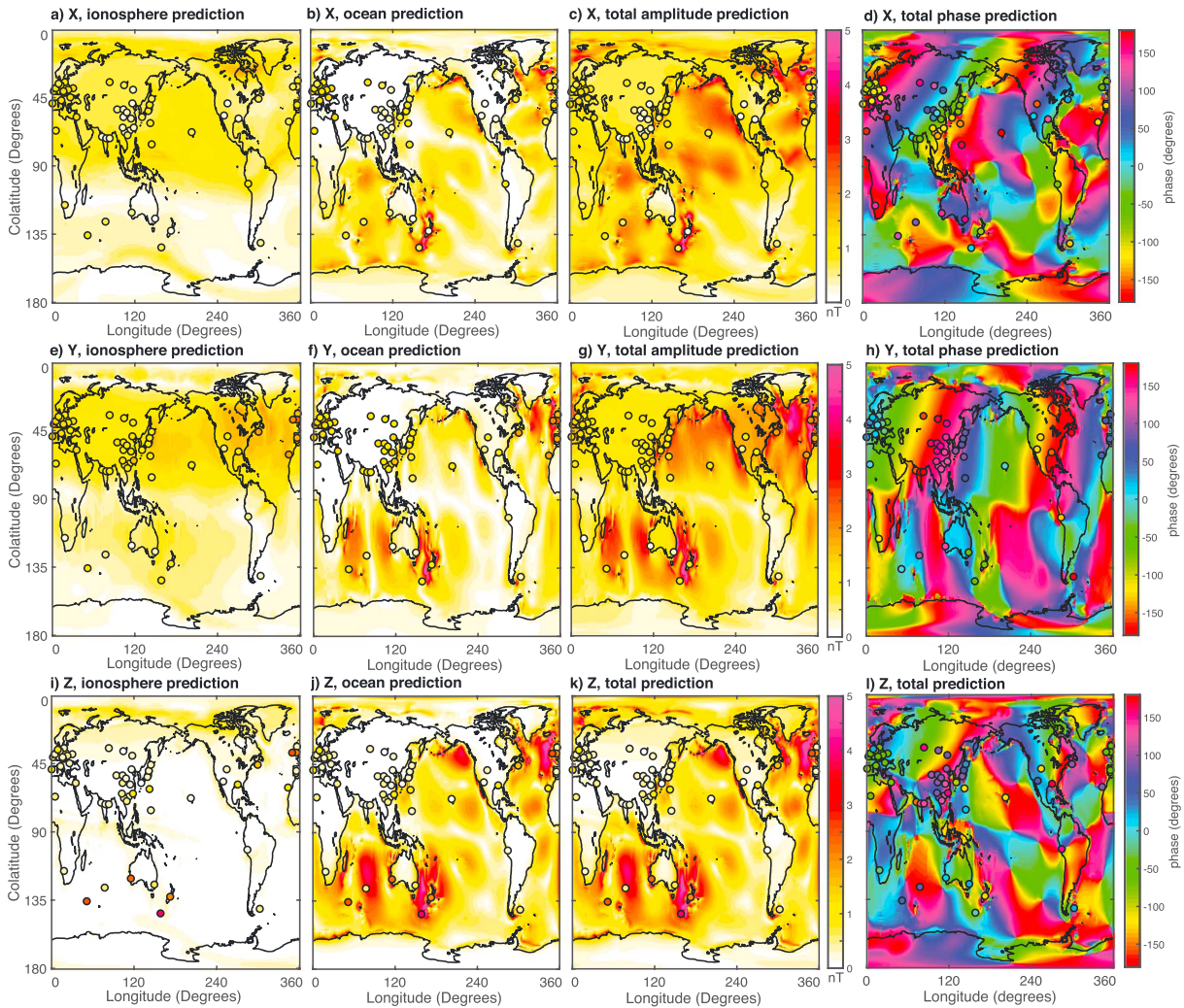


Figure 2. For the leftmost column, the background map illustrates the (a) X, (e) Y, and (i) Z component magnetic amplitudes predicted from the ionospheric tidal source. The second column depicts the (b) X, (f) Y, and (j) Z component magnetic amplitudes predicted from the oceanic tidal source. (c, g, k) The amplitude and (d, h, l) total predicted phase of the sum of the ionospheric and oceanic components. Each colored dot represents the M_2 amplitude or phase estimated at a geomagnetic observatory for the corresponding component.

and magnetic (\mathbf{B}) fields excited by an electric source in a spherical model of Earth that has a three-dimensional (3-D) distribution of electrical conductivity. Within this numerical solution, Maxwell's equations in the frequency domain

$$\frac{1}{\mu_0} \nabla \times \mathbf{B} = \sigma \mathbf{E} + \mathbf{j}^{\text{ext}} \quad (2)$$

and

$$\nabla \times \mathbf{E} = i\omega \mathbf{B}, \quad (3)$$

are reduced to an integral equation with a contracting kernel (e.g., Pankratov et al., 1995). Here \mathbf{j}^{ext} represents the complex-valued, exciting current (i.e., \mathbf{j}^{ext} is the electric current induced by the tidal flow from either the ocean, $\mathbf{j}_{\text{ocean}}^{\text{ext}}$, or the ionosphere, $\mathbf{j}_{\text{iono}}^{\text{ext}}$ —discussed in the following sections), σ is the model's conductivity distribution in the Earth, μ_0 is the magnetic permeability of the free space, and ω is an angular frequency. The boundary conditions used for \mathbf{E} and \mathbf{B} set both signals to 0 at the center of the Earth and at infinity. After solving the integral equation, the electric and magnetic fields at the observation points are determined using Green's function formalism. See Kuvshinov and Olsen (2004) and Kuvshinov (2008) for a more detailed description of the 3-D EM simulation for motionally induced signals.

Earth's 3-D electrical conductivity model was composed of a thin spherical layer of laterally varying conductance at the Earth's surface with radially symmetric spherical conductivity underneath. The surface conductance distribution was obtained from Manoj et al. (2006) and incorporates contributions from seawater and sediments. For the underlying laterally homogeneous spherical conductor, we used the model from Grayver et al. (2017).

Our simulations were performed at sea level using the RMACC Summit supercomputer (Anderson et al., 2017). Each simulation produced a grid of predicted magnetic field vector (\mathbf{B}) containing the X , Y , and Z components' real and imaginary parts, so that the amplitude and phase for each component may be determined (phase was determined using $\tan^{-1}(\Im P/\Re P)$, where P stands for the corresponding component of the predicted magnetic field and \Re and \Im , respectively, denote the real and imaginary parts). To properly compare the simulated scalar fields with those observed, the predicted magnetic vector \mathbf{B} was projected onto the unit vector $\frac{\mathbf{B}^m}{|\mathbf{B}^m|}$ in the direction of the main magnetic field, \mathbf{B}^m (as determined by the International Geomagnetic Reference Field), at each grid point:

$$\Delta F = \mathbf{B} \cdot \frac{\mathbf{B}^m}{|\mathbf{B}^m|}. \quad (4)$$

Figure 1 illustrates the total M_2 field predicted from the combined ionospheric and ocean sources.

3.1. Model Prediction of the M_2 Oceanic Exciting Current

The ocean-source simulations were done on a $0.25^\circ \times 0.25^\circ$ grid. The oceanic exciting current, $\mathbf{j}_{\text{ocean}}^{\text{ext}}$, is calculated as

$$\mathbf{j}_{\text{ocean}}^{\text{ext}} = \delta(r - a)\sigma_w(\mathbf{U} \times \mathbf{B}^m), \quad (5)$$

where δ is Dirac's delta function, a is Earth's mean radius, r is distance from the Earth's center, σ_w is the depth-averaged seawater conductivity, \mathbf{U} is the complex-valued depth integrated velocity due to ocean tides, and \mathbf{B}^m is the (ambient) main magnetic field of internal origin. We determined the depth-averaged seawater conductivity on a $0.25^\circ \times 0.25^\circ$ grid by interpolating the National Oceanic and Atmospheric Administration's World Ocean Atlas annual seawater conductivity climatology (Tyler et al., 2017) using MATLAB's function *interp2*. For \mathbf{U} , the assimilated, $0.125^\circ \times 0.125^\circ$ resolution, global tidal model HAMTIDE was similarly interpolated to the $0.25^\circ \times 0.25^\circ$ grid and thus utilized (Taguchi et al., 2014). The ambient magnetic field was derived from the World Magnetic Model (Chulliat et al., 2015).

3.2. Model Prediction of the M_2 Ionospheric Exciting Current

The ionosphere-source simulations were done on a $1^\circ \times 1^\circ$ grid. The ionospheric exciting current, $\mathbf{j}_{\text{iono}}^{\text{ext}}$, was calculated using the Whole Atmosphere Community Climate Model climatological lunar tidal simulation added to the lower boundary (32-km altitude) of the TIME-GCM (Roble & Ridley, 1994). This enabled the M_2 lunar tide to propagate through the atmosphere into the ionosphere and drive the ionospheric dynamo. As described by Richmond and Maute (2014), a spherical harmonic analysis of the resultant three-dimensional current is used to compute the ground-level magnetic effect and its associated equivalent current layer at 110 km for use as $\mathbf{j}_{\text{iono}}^{\text{ext}}$. The thermospheric M_2 lunar tide characteristics are influenced, among other things, by the middle atmosphere mean winds, which are a main factor in determining the propagation conditions (Forbes et al., 2013). Previous TIME-GCM simulations that included M_2 forcing compared favorably with observational results, indicating that the TIME-GCM mean winds are suitably accurate to correctly propagate the M_2 from the stratosphere to the lower mesosphere (Maute et al., 2016; Pedatella et al., 2014).

The model was run from 30 June to 28 July 2009—a time span that overlaps with the middle of the observational time span used. Geomagnetic activity was kept constant at a very low level, as was solar radiation ($F_{10.7} = 70$). Because we used climatological lunar tides, kept geomagnetic activity low, and used constant solar forcing, these TIME-GCM simulations are not reflective of the true 2009 conditions but instead are for idealized conditions. Simulations with and without the M_2 forcing were run, and the difference of their equivalent current was used to isolate the M_2 contribution and nonlinear effects. The equivalent current is given in the form of a current function as a $1.875^\circ \times 4.5^\circ$ latitude-longitude grid.

The equivalent current densities were determined from a current function, converted from the time domain into the frequency domain, and interpolated (using MATLAB's function *interp2*) to a $1^\circ \times 1^\circ$ grid for use in the EM induction forward modeling. Finally, to estimate the total induced magnetic signal from both the ionospheric and oceanic sources, the resulting ionospheric induced magnetic signals were interpolated to a $0.25^\circ \times 0.25^\circ$ grid to be consistent with the ocean EM induction forward modeling.

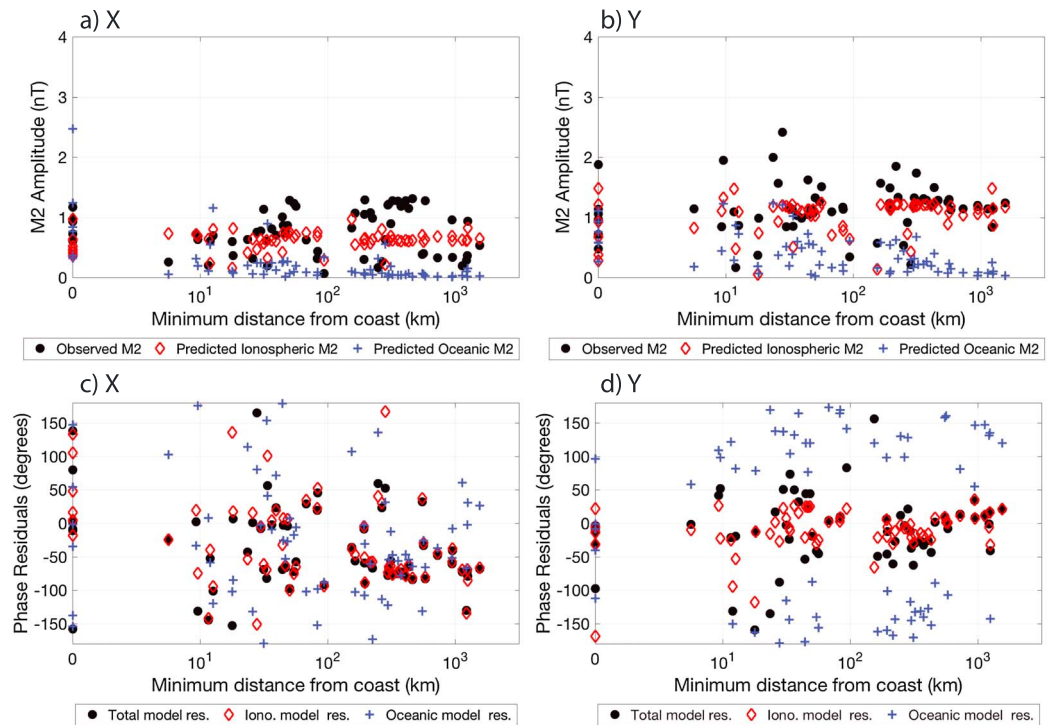


Figure 3. The observed and predicted M_2 amplitudes are plotted here dependent on their distance from the coast for (a) the X and (b) Y components (small island stations are given a distance of 0 km). Black circles denote the M_2 amplitude estimated from observations, red diamonds represent the predicted ionospheric M_2 amplitude, and blue pluses signify the predicted oceanic M_2 amplitude. The residuals between the observed and predicted M_2 phases are plotted in (c) and (d) dependent on their distance from the coast for the X and Y components (small island stations are given a distance of 0 km). Black circles denote the residual determined from the total phase (i.e., produced from the complex vector sum of the ionospheric and oceanic components), red diamonds represent the residuals from just the predicted ionospheric M_2 phases, and blue pluses signify using the predicted oceanic M_2 phases (which are meaningless inland).

4. Comparing the Predicted Ionospheric and Oceanic Signals

While the predicted oceanic M_2 amplitudes' maximum values are larger than the predicted ionospheric amplitudes, whether the ionospheric signal or oceanic signal dominates depends on both the location and the component. This is evident in Figures 2, 3a, 3b, and S2. Figure 2 compares the predicted ionospheric, oceanic, and combined (i.e., vector sum) M_2 signal with that estimated from the 64 observatories for both amplitude and phase.

Of the predicted ionospheric components, Y (Figure 2e) is the largest and Z (Figure 2i) is the smallest. The ionospheric signal's Y component and X component are both larger in the Northern Hemisphere than in the Southern Hemisphere; however, the X component has larger amplitudes coinciding with the equatorial electrojet and polar electrojets, whereas Y's amplitudes are largest in the midlatitudes (especially over North America and the North Atlantic). Similar to the X component, the ionospheric signal's Z component was larger near the equatorial and polar electrojets.

Figure 1 shows the total amplitude and phase from both the ionospheric and oceanic tidal sources. The predicted total F amplitude is very similar to that from previous studies on the oceanic M_2 magnetic signal (Grayver et al., 2016; Kuvshinov et al., 2006; Maus & Kuvshinov, 2004; Sabaka et al., 2015, 2016; Schnepf et al., 2014); however, traces of the equatorial and polar electrojets are present.

The predicted oceanic amplitudes were strongest in the Z component (Figure 2j); nonetheless, all components had larger values in the North Atlantic, the Gulf of Alaska, the Tasman Sea, and the Indian Ocean, corresponding to local maxima in the main magnetic field. Predicted oceanic signals typically quickly decrease in amplitude over continents, whereas the strength of the ionospheric signals is more dependent on the Earth's main geomagnetic field and the ionospheric conductivity magnitude (which is larger in the summer).

This is evident by comparing the columns of Figure 2, as well as evaluating Figures 3a, 3b, and S2. The latter figures compare the predicted and estimated signal amplitude at each station as a function of the station's minimum distance from the coast. The minimum distance to the coast was determined using Dan Chavas' MATLAB function *dist_from_coast* (Chavas, 2014); however, the distance to coast was set to 0 for geomagnetic stations on small islands not considered in MATLAB's coast toolbox. The largest spread between estimated and predicted M_2 amplitudes occurs either at island stations or at stations within 100 km from the coast. Moving further inland, the range in amplitudes decreases as the predicted oceanic signal drops to 0. The range in predicted ionospheric signals is almost constant across oceans and continents, and for stations further inland it is evident that the predicted ionospheric signals match the estimated amplitudes better than the near-zero oceanic signals.

The rightmost column of Figure 2 shows the X , Y , and Z phases estimated from observatories (colored dots) with the background representing the phase determined from using both the ionospheric and oceanic forward predictions (refer to Figure S4 to see the predicted ionospheric versus oceanic phase for each component). The predicted Z component oceanic M_2 phase matches those determined in Sabaka et al. (2015), and as noted in that study, the oceanic phases are effectively meaningless in continental areas where the oceanic signal goes to 0.

While the oceanic M_2 phase for each component, as well as the ionospheric M_2 Z component's phase, is highly location dependent, the ionospheric horizontal components instead are predominantly longitude dependent. This is likely because the phases were defined with respect to universal time rather than lunar time (which would instead likely be dominated by latitudinal variations). However, all ionospheric components predict a phase shift/jump occurring near the magnetic equator. Additionally, because the predicted ionospheric Z component's amplitudes are so weak, both the ionospheric and the total predicted phase for the Z component may be meaningless in continental areas.

5. Comparing the Predicted and Estimated Ionospheric and Oceanic Signals

For each component, we calculated the root-mean-square error (RMSE) between the predicted and observed M_2 amplitudes. In general, the residuals for each component followed a normal distribution. The global RMSE for F , X , Y , and Z components are ± 0.59 , ± 0.54 , ± 0.45 , and ± 0.59 nT, respectively, showing that the errors are distributed evenly between the components. However, examining the residuals in regard to the observatory's minimum distance from the coast (shown in Figure S3) revealed some interesting differences between the components. The horizontal component residuals were generally spread between -0.5 and 0.5 nT regardless of distance from the coast. Meanwhile, the F and Z residuals had a wider range at island and coastal stations—a range that sharply tapered off moving inland. For noncoastal stations, the RMSE for the F and Z components, respectively, is ± 0.36 and ± 0.25 nT, which is significantly smaller than their RMSE for coastal stations (± 0.74 and ± 0.78 nT; ± 0.62 and ± 0.69 nT if the outlying Martin de Vivies, Indian Ocean, observatory is excluded). The larger residuals in F and Z near the coast may be due to the coast effect's unexplained influence on oceanic M_2 amplitudes. Additionally, near several coastal areas, the predicted oceanic M_2 tidal amplitude dramatically changes strength over a small region, so this error may decrease using a finer model resolution for the EM induction solver. However, the oceanic M_2 magnetic signal is highly sensitive to the underlying local lithospheric and upper mantle conductivity (e.g., Schnepf et al., 2014), so model error is undoubtedly introduced by using a simple 1-D conductivity profile for the lithosphere and upper mantle. Indeed, considering our use of a relatively high-resolution grid ($0.25^\circ \times 0.25^\circ$), the discrepancy may mostly be driven by using this simplistic 1-D conductivity model.

For inland stations situated more than 100 km from the coast, the observatories do not sense oceanic M_2 magnetic signals; thus, this residual should be revealing the difference between the estimated and predicted ionospheric signal. This suggests that the error from ionospheric tidal magnetic signals is small for EM inversions using observed Z components.

As evident in Figure 2, the Y component's predicted phase best matches the observatory estimated phases. This may be because it was the component with the strongest predicted ionospheric signals, leading to good correspondence across both oceanic and continental regions. This is also shown in Figures 3 and S2, which compare the phase residual versus the observatory's distance to the coast. These figures show the residuals between the estimated phases and those predicted from the total model, as well as the ocean-only or ionospheric-only models. For the Z component (Figure S2), a second plot is made to show the residuals

at coastal stations. Aside from some outlying points, as shown in Figure 3, the Y component has the narrowest range of phase residuals (the ocean phase residuals are meaningless inland for all components).

The Z component predicted and observed phase seem to match well in coastal areas, with most stations' values being within $\pm 60^\circ$ to the predicted value (see Figures 2, S2, and S5). The larger phase residuals at the other coastal stations may also be due to our simplistic 1-D conductivity profile for the lithosphere and upper mantle.

Looking at Figure 3, the X component's phase residuals have a band that matches well across coastal/continental locations. Some of the coastal outliers may be due to unmodeled coastal effects on the predicted oceanic M_2 signal. However, what is curious are the large residuals between the continental observatories' estimated and predicted phases—for example, all of the European observatories have residuals between -50 and -100° . It seems that there may be an unexplained or unmodeled ionospheric process causing this discrepancy.

The scalar anomaly's predicted phase and observed phase (shown in Figure 1b) match well for most of the Northern Hemisphere; yet there are obvious deviations that coincide with observatories that have a small estimated F amplitude. It is interesting that for the scalar anomaly, the phase in coastal areas matches poorly compared to the X , Y , and Z components (see Figure S2). For areas such as eastern Asia, which had good phase agreement for the individual components, the deviations may be due to using 1-D rather than 3-D conductivity model or some other physical process. Meanwhile, some of the in-land stations in North Africa and East Asia with large F phase residuals also had large phase residuals for the X component, perhaps also due to an unexplained or unmodeled ionospheric process.

It is worth noting that the observed ionospheric amplitudes are much stronger than what would be observed if only local nighttime data were used. Schnepf et al. (2014) compared the daytime and nighttime M_2 amplitudes from seafloor magnetometer stations and found that the nighttime estimates were generally 10–30% smaller than the daytime estimates. How well the simulations' nighttime predictions match the observatories' local nighttime ionospheric amplitudes is not shown in this study.

6. Conclusions and Outlook

We compared M_2 magnetic signals estimated from global observatories to physics-based numerical models of the ionospheric M_2 magnetic field and the oceanic M_2 magnetic field. Specifically, this study used TIME-GCM's ionospheric M_2 electric current to provide a first comparison of the predicted ionospheric M_2 electric current's induced magnetic field with M_2 amplitudes and phases estimated from observatories across the globe. We found that the TIME-GCM's ionospheric M_2 electric current generally provided a prediction of the ionospheric M_2 amplitudes that was often within ± 0.5 nT of the observatory's estimate—a remarkable result considering the complexity of the ionospheric tidal signal. We found good agreement in the phases for the Y component and discrepancies in the F and X component's phase, possibly due to unmodeled processes. Meanwhile, the ionospheric Z component's phase is effectively meaningless due to the small Z amplitudes. Discrepancies in amplitudes and phases at coastal regions may be due to the unmodeled coast effect as well as limitations due to the model's resolution. However, considering that we used a $0.25^\circ \times 0.25^\circ$ grid for the ocean signal modeling, it seems most likely that incorporating local changes in lithospheric and upper mantle conductivity would be most useful for decreasing the residuals between observatory estimates and predictions at these sites.

By focusing on a time period encompassing the Northern Hemisphere's summer, we avoided the possibility of SSWs influencing observed tidal signals. The focus time period was during a solar minimum, thereby minimizing magnetospheric effects on the ionospheric signal. However, there still are many other relevant factors in determining the strength of the ionospheric tidal signal, so it is a promising start that a climatological model fits the data this well. Future investigations may improve the fit between observations and models by using actual geomagnetic and solar radiation conditions as input for running TIME-GCM or investigating other variables relevant to the strength of ionospheric tidal currents. Additionally, while this 90-day time period was ideal for space weather conditions, a longer time series would minimize the error of the estimated observatory signals.

The smallness of the ionospheric tidal field's modeled vertical component (Z) is very encouraging for EM sensing. For studies using satellite data for tidal EM sensing (e.g., Grayver et al., 2016, 2017), only the vertical

component (Z) is used, and it was assumed that this signal is of pure oceanic origin. This was confirmed by our modeling, which provided negligible tidal Z signals of ionospheric origin. However, it is worthwhile to note that studies using seafloor data for EM sensing may also use the horizontal field components for conductivity inversions, and these components have significant ionospheric signals. Because our study focused on a time period when the ionospheric signals were weaker, our results effectively provide a lower error bound for EM sensing that cannot separate out local nighttime data. Additional work may refine this error by considering different time periods and different climatologies.

Acknowledgments

The authors would like to thank the reviewers for useful feedback. N. R. S. would like to thank K. F. Tiampo, A. F. Sheehan, B. M. Jakosky, R. Bilham, and S. Zhong for useful discussions. N. R. S. was supported by NASA grant 80NSSC17K0450. N. R. S. and M. N. were also supported by a CIRES IRP grant. A. M. and A. D. R. were supported by NASA grant NNX13AF77G and NSF grant AGS-1135446. The National Center for Atmospheric Research is sponsored by the National Science Foundation. TIME-GCM results are archived on the National Center for Atmospheric Research High Performance Storage System and are available upon request. The predicted ionospheric and oceanic M_2 magnetic tidal signals at sea level were computed using the RMACC Summit supercomputer, which is supported by the National Science Foundation (awards ACI-1532235 and ACI-1532236), the University of Colorado Boulder, and Colorado State University. The Summit supercomputer is a joint effort of the University of Colorado Boulder and Colorado State University. Results are available at geomag.colorado.edu/IOMS-M2. A. M. would like to acknowledge high-performance computing support from Yellowstone ([ark:/85065/d7wd3xhc](https://doi.org/10.1029/2018GL078487)) provided by NCAR's Computational and Information Systems Laboratory, sponsored by the National Science Foundation.

References

- Anderson, J., Burns, P. J., Milroy, D., Ruprecht, P., Hauser, T., & Siegel, H. J. (2017). Deploying RMACC Summit: An HPC Resource for the Rocky Mountain Region. In Proceedings of PEARC17 (7 pp.). New Orleans, LA, USA, July 09-13, 2017. <https://doi.org/10.1145/3093338.3093379>
- Bindoff, N. L., Lilley, F. E. M., & Filloux, J. H. (1988). A separation of ionospheric and ocean tidal components in magnetic fluxuation data. *Journal of Geomagnetism and Geoelectricity*, *40*, 1445–1467.
- Chau, J. L., Hoffmann, P., Pedatella, N. M., Matthias, V., & Stober, G. (2015). Upper mesospheric lunar tides over middle and high latitudes during sudden stratospheric warming events. *Journal of Geophysical Research: Space Physics*, *120*, 3084–3096. <https://doi.org/10.1002/2015JA020998>
- Chavas, D. (2014). `dist_from_coast`.
- Chulliat, A., Macmillan, S., Alken, P., Beggan, C., Nair, M., Hamilton, B., et al. (2015). The US/UK world magnetic model for 2015–2020 (Tech. Rep.) Boulder, CO: NOAA National Geophysical Data Center. <https://doi.org/10.7289/V5TH8JNW>
- Civet, F., & Tarits, P. (2013). Analysis of magnetic satellite data to infer the mantle electrical conductivity of telluric planets in the solar system. *Planetary and Space Science*, *84*, 102–111. <https://doi.org/10.1016/j.pss.2013.05.004>
- Civet, F., Thébaud, E., Verhoeven, O., Langlais, B., & Saturnino, D. (2015). Electrical conductivity of the Earth's mantle from the first Swarm magnetic field measurements. *Geophysical Research Letters*, *42*, 3338–3346. <https://doi.org/10.1002/2015GL063397.1>
- Cueto, M., Mcknight, D., & Herraiz, M. (2003). Daily geomagnetic variations on the Iberian Peninsula. *Geophysical Journal International*, *152*, 113–123.
- Denig, W. F. (2015). Geomagnetic K_p and A_p indices.
- Egbert, G. D., & Erofeeva, S. Y. (2002). Efficient inverse modeling of barotropic ocean tides. *Journal of Atmospheric and Oceanic Technology*, *19*, 183–204.
- Forbes, J. M. (1996). Planetary waves in the thermosphere-ionosphere system. *Journal of Geomagnetism and Geoelectricity*, *48*, 91–98.
- Forbes, J. M., Zhang, X., Bruinsma, S., & Oberheide, J. (2013). Lunar semidiurnal tide in the thermosphere under solar minimum conditions. *Journal of Geophysical Research: Space Physics*, *118*, 1788–1801. <https://doi.org/10.1029/2012JA017962>
- Grayver, A. V., Munch, F. D., Kuvshinov, A. V., Khan, A., & Sabaka, T. J. (2017). Joint inversion of satellite-detected tidal and magnetospheric signals constrains electrical conductivity and water content of the upper mantle and transition zone. *Geophysical Research Letters*, *44*, 6074–6081. <https://doi.org/10.1002/2017GL073446>
- Grayver, A. V., Schnepf, N. R., Kuvshinov, A. V., Sabaka, T. J., Mano, C., & Olsen, N. (2016). Satellite tidal magnetic signals constrain oceanic lithosphere-asthenosphere boundary. *Science Advances*, *2*, e1600798.
- Hewson-Browne, R. C. (1973). Magnetic effects of sea tides. *Physics of the Earth and Planetary Interiors*, *7*, 161–166.
- Kelley, M. C. (1989). *The Earth's ionosphere: Plasma physics and electrodynamics*. San Diego, CA: Academic Press Inc.
- Kuvshinov, A. V. (2008). 3-D global induction in the oceans and solid Earth: Recent progress in modeling magnetic and electric fields from sources of magnetospheric, ionospheric and oceanic origin. *Surveys in Geophysics*, *29*(2), 139–186. <https://doi.org/10.1007/s10712-008-9045-z>
- Kuvshinov, A., Junge, A., & Utada, H. (2006). 3-D modelling the electric field due to ocean tidal flow and comparison with observations. *Geophysical Research Letters*, *33*, L06314. <https://doi.org/10.1029/2005GL025043>
- Kuvshinov, A., & Olsen, N. (2004). 3-D modelling of the magnetic fields due to ocean tidal flow, *CHAMP mission results II* (pp. 359–365). Berlin: Springer.
- Larsen, J. C. (1968). Electric and magnetic fields induced by deep sea tides. *The Geophysical Journal of the Royal Astronomical Society*, *16*, 47–70.
- Larsen, J., & Cox, C. (1966). Lunar and solar daily variation in the magnetotelluric field beneath the ocean. *Journal of Geophysical Research*, *71*(18), 4441–4445.
- Love, J. J., & Rigler, E. J. (2014). The magnetic tides of Honolulu. *Geophysical Journal International*, *197*, 1335–1353. <https://doi.org/10.1093/gji/ggu090>
- Malin, S. R. C. (1970). Separation of lunar daily geomagnetic variations into parts of ionospheric and oceanic origin. *The Geophysical Journal of the Royal Astronomical Society*, *21*, 447–455.
- Manoj, C., Kuvshinov, A., & Maus, S. (2006). Ocean circulation generated magnetic signals. *Earth Planets Space*, *58*, 429–437.
- Maus, S., & Kuvshinov, A. (2004). Ocean tidal signals in observatory and satellite magnetic measurements. *Geophysical Research Letters*, *31*, L15313. <https://doi.org/10.1029/2004GL020090>
- Maute, A., Fejer, B. G., Forbes, J. M., Zhang, X., & Yudin, V. (2016). Equatorial vertical drift modulation by the lunar and solar semidiurnal tides during the 2013 sudden stratospheric warming. *Journal of Geophysical Research: Space Physics*, *121*, 1658–1668. <https://doi.org/10.1002/2015JA022056>
- McKnight, J. D. (1995). Lunar daily geomagnetic variations in New Zealand. *Geophysical Journal International*, *122*, 889–898.
- Olsen, N., Friis-Christensen, E., Floborghagen, R., Alken, P., Beggan, C. D., Chulliat, A., et al. (2013). The Swarm satellite constellation application and research facility (SCARF) and Swarm data products. *Earth, Planets and Space*, *65*(c), 1189–1200. <https://doi.org/10.5047/eps.2013.07.001>
- Pankratov, O., Avdeev, D., & Kuvshinov, A. (1995). Electromagnetic field scattering in a homogeneous Earth: A solution to the forward problem. *Physics of the Solid Earth*, *31*, 201–209.
- Pediatella, N. M. (2014). Observations and simulations of the ionospheric lunar tide: Seasonal variability. *Journal of Geophysical Research: Space Physics*, *119*, 5800–5806. <https://doi.org/10.1002/2014JA020189>
- Pediatella, N. M., Liu, H., & Richmond, A. D. (2012). Atmospheric semidiurnal lunar tide climatology simulated by the whole atmosphere community climate model. *Journal of Geophysical Research*, *117*, A06327. <https://doi.org/10.1029/2012JA017792>

- Pediatella, N. M., Liu, H.-L., Sassi, F., Lei, J., Chau, J. L., & Zhang, X. (2014). Ionosphere variability during the 2009 SSW: Influence of the lunar semidiurnal tide and mechanisms producing electron density variability. *Journal of Geophysical Research: Space Physics*, *119*, 3828–3843. <https://doi.org/doi:10.1002/2014JA019849>
- Püthe, C., & Kuvshinov, A. (2013). Determination of the 3-D distribution of electrical conductivity in Earth's mantle from Swarm satellite data: Frequency domain approach based on inversion of induced coefficients. *Earth, Planets and Space*, *65*, 1247–1256. <https://doi.org/10.5047/eps.2013.09.004>
- Püthe, C., & Kuvshinov, A. (2014). Mapping 3-D mantle electrical conductivity from space: A new 3-D inversion scheme based on analysis of matrix Q-responses. *Geophysical Journal International*, *197*, 768–784. <https://doi.org/10.1093/gji/ggu027>
- Püthe, C., Kuvshinov, A., Khan, A., & Olsen, N. (2015). A new model of Earth's radial conductivity structure derived from over 10 yr of satellite and observatory magnetic data. *Geophysical Journal International*, *203*, 1864–1872. <https://doi.org/10.1093/gji/ggv407>
- Richmond, A. D. (1995). Modeling equatorial ionospheric electric field. *Journal of Atmospheric and Terrestrial Physics*, *57*, 1103–1115.
- Richmond, A. D., & Maute, A. (2014). Ionospheric electrodynamics modeling. In J. Huba, R. Schunk, & G. Khazanov (Eds.), *Modeling the Ionosphere-Thermosphere System* (pp. 57–71). Chichester, UK: John Wiley. <https://doi.org/10.1002/9781118704417.ch6>
- Roble, R. G., & Ridley, E. C. (1994). A thermosphere-ionosphere-mesosphere-electrodynamics general circulation model (TIME-GCM): Equinox solar cycle minimum simulations (30–500 km). *Geophysical Research Letters*, *21*(6), 417–420.
- Sabaka, T. J., Olsen, N., Tyler, R. H., & Kuvshinov, A. (2015). CM5, a pre-Swarm comprehensive geomagnetic field model derived from over 12 yr of CHAMP, Ørsted, SAC-C and observatory data. *Geophysical Journal International*, *200*, 1596–1626. <https://doi.org/10.1093/gji/ggu493>
- Sabaka, T. J., Tyler, R. H., & Olsen, N. (2016). Extracting ocean-generated tidal magnetic signals from Swarm data through satellite gradiometry. *Geophysical Research Letters*, *43*, 3237–3245. <https://doi.org/10.1002/2016GL068180>.Received
- Schnepf, N. R., Kuvshinov, A., & Sabaka, T. J. (2015). Can we probe the conductivity of the lithosphere and upper mantle using satellite tidal magnetic signals? *Geophysical Research Letters*, *42*, 3233–3239. <https://doi.org/10.1002/2015GL063540>
- Schnepf, N. R., Manoj, C., Kuvshinov, A., Toh, H., & Maus, S. (2014). Tidal signals in ocean-bottom magnetic measurements of the Northwestern Pacific: Observation versus prediction. *Geophysical Journal International*, *198*, 1096–1110. <https://doi.org/10.1093/gji/ggu190>
- Stening, R. J. (2011). Lunar tide in the equatorial electrojet in relation to stratospheric warmings. *Journal of Geophysical Research*, *116*, A12315. <https://doi.org/10.1029/2011JA017047>
- Taguchi, E., Stammer, D., & Zahel, W. (2014). Inferring deep ocean tidal energy dissipation from the global high-resolution data-assimilative HAMTIDE model. *Journal of Geophysical Research: Oceans*, *119*, 4573–4592. <https://doi.org/10.1002/2013JC009766>
- Tyler, R. H., Boyer, T. P., Minami, T., Zweng, M. M., & Reagan, J. R. (2017). Electrical conductivity of the global ocean. *Earth, Planets and Space*, *69*, 156. <https://doi.org/10.1186/s40623-017-0739-7>
- Tyler, R. H., Maus, S., & Lühr, H. (2003). Satellite observations of magnetic fields due to ocean tidal flow. *Science*, *299*(5604), 239–241. <https://doi.org/10.1126/science.1078074>
- Velínský, J. (2010). Electrical conductivity in the lower mantle: Constraints from CHAMP satellite data by time-domain EM induction modelling. *Physics of the Earth and Planetary Interiors*, *180*, 111–117. <https://doi.org/10.1016/j.pepi.2010.02.007>
- Velínský, J. (2013). Determination of three-dimensional distribution of electrical conductivity in the Earth's mantle from Swarm satellite data: Time-domain approach. *Earth, Planets and Space*, *65*, 1239–1246. <https://doi.org/10.5047/eps.2013.08.001>
- Winch, D. E. (1970). Geomagnetic lunar partial tides. *Journal of Geomagnetism and Geoelectricity*, *22*(3), 291–318.
- Winch, D. E. (1981). Spherical harmonic analysis of geomagnetic tides, 1964–1965. *Philosophical Transactions of the Royal Society of London*, *303*, 1–104.
- Yamazaki, Y., & Kosch, M. J. (2014). Geomagnetic lunar and solar daily variations during the last 100 years. *Journal of Geophysical Research: Space Physics*, *119*, 6732–6744. <https://doi.org/10.1002/2014JA020203>
- Zhang, J. T., & Forbes, J. M. (2013). Lunar tidal winds between 80 and 110 km from UARS/HRDI wind measurements. *Journal of Geophysical Research: Space Physics*, *118*, 5296–5304. <https://doi.org/10.1002/jgra.50420>